Research Square

Preprints are preliminary reports that have not undergone peer review.
They should not be considered conclusive, used to inform clinical practice,
or referenced by the media as validated information.

# Experimental Study on Robotic Eddy Current Inspection of Aeroengine Turbine Blades

**Kai Song**
Nanchang Hangkong University
**Wenyu Xie**
Nanchang Hangkong University
**Wenbo Zhou**
Aero Engine Corporation of China Power Corporation Ltd.
**Yuhua You**
Nanchang Hangkong University
**Junxian Liu**
Nanchang Hangkong University
**Rongbiao Wang**
wangrongbiao@nchu.edu.cn
Nanchang Hangkong University

**Research Article**

**Keywords:** Automated detection, Eddy current testing, Subsurface defects, Trajectory planning, Turbine blade

**Posted Date:** July 10th, 2026

**DOI:** https://doi.org/10.21203/rs.3.rs-9127018/v1

**License:** This work is licensed under a Creative Commons Attribution 4.0 International License.
Read Full License

**Additional Declarations:** No competing interests reported.

# Experimental Study on Robotic Eddy Current Inspection of Aeroengine Turbine Blades

Kai Song[1], Wenyu Xie[1], Wenbo Zhou[2], Yuhua You[1], Junxian Liu[1], Rongbiao Wang[1]

**Abstract**
This study proposes an automated eddy current inspection technology to address the challenges in detecting subsurface cold-shut defects in aero-engine turbine blades. First, based on the principle of eddy current testing, an optimal bridge absolute probe configuration was designed through electromagnetic field finite element simulation to optimize the magnetic core materials and coil parameters, thereby eliminating blind detection zones in manual operations. Second, a robot-turntable cooperative inspection system is constructed to develop an automated prototype. Finally, trajectory planning was implemented using a standard notched specimen to analyze the influence of the robot motion parameters, defect depth, and orientation on the signal characteristics. A comprehensive verification of the detection capability of the system was conducted via experiments on real cracked blades. This technology significantly enhances the efficiency and reliability of turbine blade defect detection, providing critical assurance for the safe operation of aeroengines.

**Index Terms** Automated detection· Eddy current testing· Subsurface defects· Trajectory planning· Turbine blade

## 1 Introduction

The aeroengine, as the core power component of an aircraft[1], its stability directly determines flight safety and national industrial strength[2]. As a core high-temperature and high-pressure component of an engine[3], the turbine blade must operate under complex stresses[4]. During the precision casting process, subsurface and internal metallurgical defects such as cold shut and shrinkage are prone to occur, severely affecting the engine's performance and safety[5]. Fig. 1 shows a schematic of the aeroengine and its blank turbine blade.

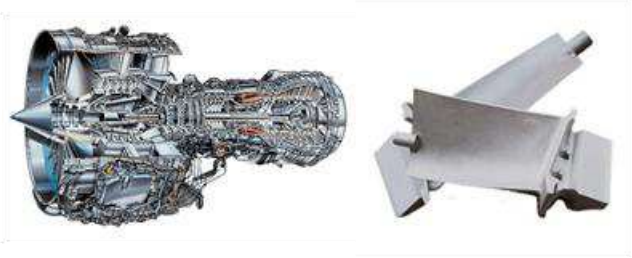


**Fig. 1** Example of aeroengine and blank power turbine blade

Traditional nondestructive testing techniques (such as ultrasonic, radiographic, and fluorescent penetrant testing) are suitable for detecting internal/surface open defects[6]. However, they are inefficient in detecting subsurface defects like cold shut at the exhaust edge of turbine blades. Manual eddy current testing is challenging owing to limitations such as low efficiency, large blind zones, and poor positioning accuracy[7,8]. With the integration of Industry 4.0 and digital twin technology, automated robotic eddy current testing systems will become a core tool for quality control throughout the entire lifecycle of turbine blades, significantly improving detection efficiency, reducing costs, enhancing safety, and promoting the transformation of aerospace manufacturing towards a "data-driven" approach. Fig. 2 shows an example of a cold shut defect detected by fluorescent penetrant testing.



**Fig. 2** Cold shut defect display of turbine blade

Turbine blade casting is prone to defects such as inclusions, shrinkage, and cold shut[9]-[12], which significantly increases the risk of operational failures and requires comprehensive management using nondestructive testing technologies. Eddy current testing plays a key role in surface and subsurface defects. P. Lv[13] proposed a theoretical calculation method that solved the eddy current force in the process of non-ferrous metal sorting and proved its correctness using the finite element method. J. Ge[14] improved the eddy current imaging

Corresponding author
Rongbiao Wang
e-mail: 1579399122@qq.com; 89425434@qq.com; wangrongbiao@nchu.edu.cn

[1] Nanchang Hangkong University, Nanchang 330063，China.
[2] Aero Engine Corporation of China Power Corporation Ltd., Zhuzhou 412002, China.

method using rotating eddy current testing signals, enhanced the clarity of surface defect profiles, and demonstrated stable performance in detecting cracks at different angles and depths. A. V. Egorov[15] employed multi-frequency eddy current testing combined with principal component analysis to effectively mitigate the influence of probe pressure variations, thereby enhancing the accuracy of eddy current testing. J. Yuan[16] This paper establishes a finite element model to investigate the influence of coil parameters and crack parameters on eddy current signals, providing a theoretical basis and reference value for the design and optimization of eddy current probes used in detecting surface cracks on turbine blades. H. B. Zhang[17] proposed a detection transformer method based on a multi-scale fusion attention mechanism, which is designed to address the challenges of multi-scale defect detection and imbalanced sample issues in the context of aeroengine turbine blade casting defect inspection.

This study addresses the challenge of detecting subsurface cold shut defects at the exhaust edge of turbine blades in aeroengines and proposes an automated imaging detection method based on eddy current testing. The research optimizes the probe structure and parameters for small space blind zones through electromagnetic field finite element simulation, and designs an automated detection system that coordinates robots and a Programmable Logic Controller (PLC). A systematic comparison is conducted to determine the optimal scanning method, standard samples are made to verify the detection capability, and the effects of motion parameters and defect characteristics on the detection results are analyzed. Ultimately, the system's detection performance for real natural defects is verified, with a blind zone of ≤ 1.5 mm. This provides an efficient and reliable automated detection technology for turbine blade quality control with a significant engineering application value.

## 2 Eddy current testing theory

Eddy current testing (ECT) is a nondestructive testing method based on the principle of electromagnetic induction[18], primarily used for detecting surface and subsurface defects in conductive metals and some non-metallic materials. The principle is as follows: when an alternating current is passed through a detection coil, it generates an alternating magnetic field. According to Faraday's law of electromagnetic induction, an alternating magnetic field induces an eddy current field on the workpiece surface being inspected. The distribution and intensity of the eddy current field are influenced by parameters such as size, shape, conductivity, and magnetic permeability of the workpiece. The variation in the eddy current field subsequently affects the magnetic flux of the induced magnetic field, leading to a change in the impedance of the detection coil [19]. By detecting this impedance change, defect information regarding the surface and subsurface of the workpiece can be indirectly obtained, as shown in Fig. 3.

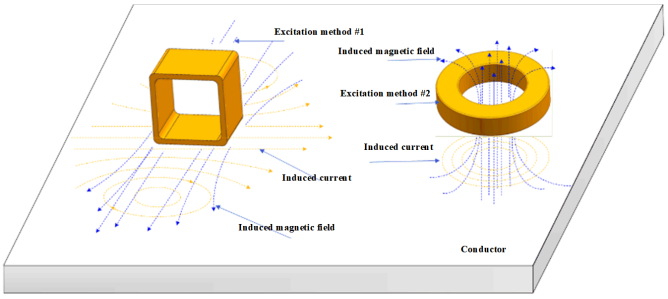



**Fig. 3** Schematic diagram of ECT

The theory of Maxwell's Equations originates from the accumulation of electromagnetic research in Europe from the late 18th century to the mid-19th century. In 1873, Maxwell, based on the works of predecessors, constructed a framework for electromagnetic equations in quaternion form. Later, Heaviside and Gibbs reformulated them using vector analysis and integrated them into a differential-integral form, ultimately forming the core of classical electromagnetic theory—the Maxwell Equations, consisting of four equations—which laid the theoretical foundation for the unified description of electromagnetic fields.

$$\oint_A E \cdot da = \frac{Q}{\varepsilon_0} \tag{1}$$

$$\oint_A B \cdot da = 0 \tag{2}$$

$$\oint_L E \cdot dl = -\frac{\delta}{\delta t}\int_A B \cdot da \tag{3}$$

$$\oint_L B \cdot dl = \mu_0 I + \mu_0 \varepsilon_0 \frac{\delta}{\delta t}\int_A E \cdot da \tag{4}$$

In electromagnetic induction, the conductor is excited by an alternating magnetic field, generating layered eddy currents that which can be equivalently represented as a secondary loop magnetically coupled with the excitation coil. Based on the impedance analysis theory, the detection signal is analyzed by establishing a mapping relationship between the induced voltage in the coil and the variations in the inductance-resistance parameters. According to Kirchhoff's law, the primary excitation current I1 induces a secondary current I2 in the conductor, and its distribution characteristics directly reflect the electromagnetic properties and potential defect information of the material:

$$\begin{cases} R_1\dot{I}_1 + j\omega L_1\dot{I}_1 - j\omega M\dot{I}_2 = \dot{U} \\ R_2\dot{I}_2 + j\omega L_2\dot{I}_2 - j\omega M\dot{I}_1 = 0 \end{cases} \tag{5}$$

In the formula, $R_1$ and $R_2$ represent the equivalent resistance of the coil, $U$ represents the excitation voltage, $\omega$ represents the excitation voltage angular frequency, $M$ represents the mutual inductance coefficient, which is related to the coupling degree between the two. The no-load impedance of the primary coil can be expressed as:

$$Z_{11} = R_1 + jX_1 \tag{6}$$

In the formula, $X_1$ is the inductive reactance of the primary coil, and the self-impedance of the secondary coil is:

$$Z_{22} = R_2 + jX_2 \tag{7}$$

$X_2$ is the inductive reactance of the eddy current loop formed on the surface of the workpiece. The coupling impedance between the primary coil and the detection object is:

$$Z_{12} = jX_M \tag{8}$$

$X_M = \omega M$ is the coupling inductive reactance. Then, the KVL equation can be simplified as:

$$\begin{cases} Z_{11}I_1 - Z_{12}I_2 = U \\ Z_{22}I_2 - Z_{12}I_1 = 0 \end{cases} \tag{9}$$

It reflects the effect of the surface condition of the workpiece on the detection coil. Therefore, the detection circuit model can be simplified to a single equivalent detection coil loop, as shown in Fig. 4, making the impedance analysis method more straightforward.

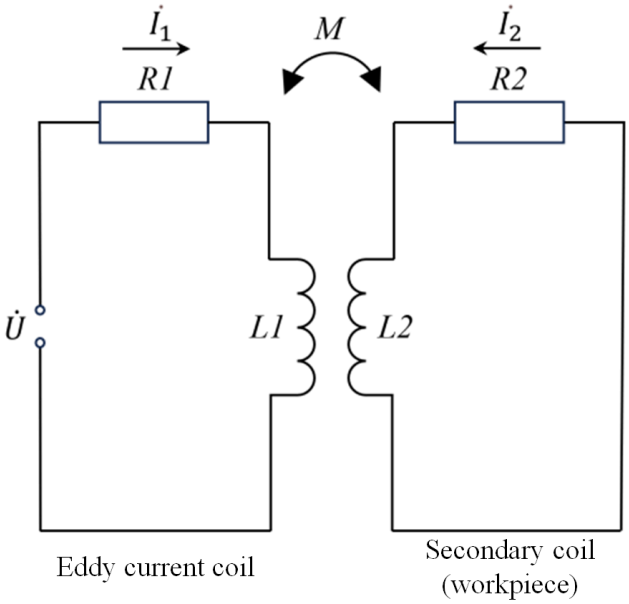



**Fig. 4** Equivalent circuit of ECT

## 3 Simulation of blade probe

### 3.1Model establishment

Turbine blade subsurface cold shut defects are commonly found in the exhaust edge region, and the natural defect direction is uncertain. As shown in Fig. 5, fluorescence detection reveals that a cold shut defect on a certain blade is located near the lower edge of the exhaust side, with the main body of the defect nearly parallel to the exhaust edge, resulting in a weak signal from the differential eddy current detection coil. Considering the actual working conditions, a circular absolute-type coil structure was selected, and further simulation tests were conducted.

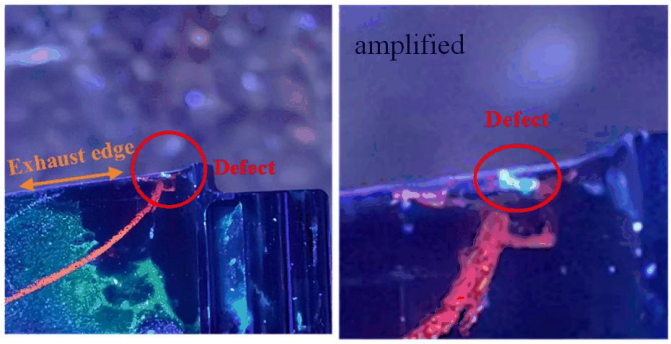



**Fig. 5** Schematic diagram of fluorescent detection of a real cold shut defect

Circular bridge absolute edge detection simulation model based on COMSOL Multiphysics (Fig. 6).

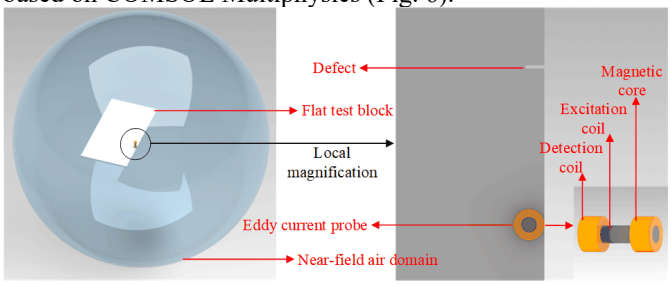



**Fig. 6** Circular bridge absolute coil edge simulation model

The model includes detection/excitation coils, a magnetic core, a nickel-based high-temperature alloy flat plate test piece, artificial groove defects, and a near-field air domain. For the smooth characteristics of the turbine blade exhaust edge, the flat plate test piece is set with dimensions of 30 mm (length) × 15 mm (width) × 0.5 mm (thickness), with a pre-fabricated artificial defect at the edge of 0.6 mm (length) × 0.1 mm (width) × 0.5 mm (depth). To ensure calculation accuracy, the near-field air domain was modeled as a three-dimensional sphere with a radius of 40 mm. The specific parameter values are summarized in Table 1.

Table 1 Summary of provisional dimensions for each part of the simulation model

| Unit name | Dimension parameters | Numerical value (units : mm) |
|---|---|---|
| Detection coil | $r_1$、$R_1$、$H_1$、$N_1$ | 0.5、1.2、1、150 |
| *Excitation coil* | $r_2$、$R_2$、$H_2$、$N_2$ | 0.5、1.2、1、150 |
| *Magnetic core* | $r_4$、$h_1$ | 0.25、3 |
| *Nickel-based high-temperature alloy flat plate* | L、W、T | 30、15、0.5 |
| *Artificial groove defect* | l、w、d | 0.6、0.1、0.5 |

The detection coil (inner and outer radii ( r1/R1 ), height (

H1 ), number of turns ( N1 )) and excitation coil (inner and outer radii ( r2/R2 ), height ( H2 ), number of turns ( N2 ), and wire diameter ( r3 )) are coupled by a cylindrical magnetic core (radius ( r4 ), length ( h1 )). The coil spacing is ( h2 ), and the distance from the detection coil to the workpiece surface is ( h3 ).

Some of the dimensional parameters correspond to the situation shown in Fig. 7. The probe was moved along the edge of the flat plate test piece and perpendicular to the length direction of the artificial groove defect. The simulation excitation frequency ( f ) and excitation voltage ( V ) were tentatively set to 1.25 MHz and 5V, respectively.

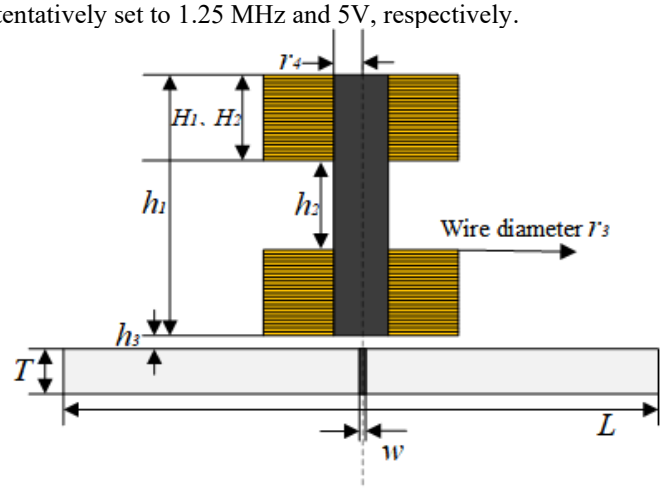



**Fig. 7** Schematic diagram of simulation model cross-section parameters

As shown in Fig. 8, the mesh division results of the model, excluding the near-field air domain, are illustrated, and the mesh division results for the near-field air doma

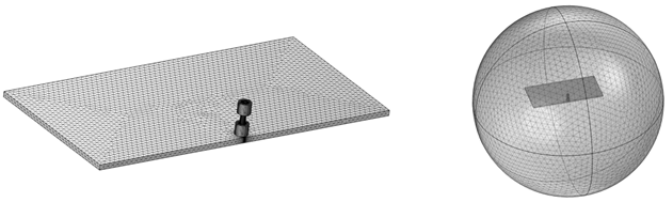


**Fig. 8** Mesh division result of the main model and the near-field air domain

### 3.2 Influence of inspection process parameters on detection signals

The eddy current detection performance of permalloy 1J85 and manganese-zinc ferrite magnetic cores was compared. The high magnetic permeability of the core enhances the concentration of the magnetic field, thereby improving the sensitivity. In the simulation, the conductivity and magnetic permeability parameters were adjusted with the probe moving along the flat plate test piece under excitation conditions of 5V/1.25 MHz. The results indicate that the peak voltage of the manganese-zinc ferrite detection coil is significantly higher than that of the permalloy, with smaller signal fluctuations in the defect-free region. Considering both the dynamic characteristics and frequency domain response, manganese-zinc ferrite exhibits a superior signal-to-noise ratio (SNR) at the same frequency, as shown in the simulation results in Fig. 9.

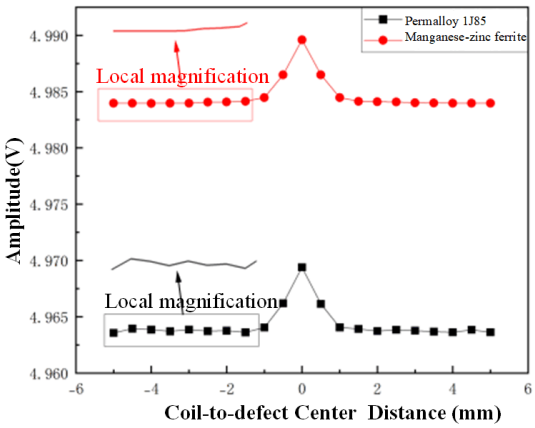



**Fig. 9** Schematic diagram of detection results for different magnetic cores

Based on Faraday's law, a manganese-zinc ferrite magnetic core was used. In the simulation, the coil turns were set to range from 100 to 250 turns (with a step size of 25 turns), a height of 1 mm, and excitation conditions of 5V/1.25 MHz. Fig. 10 shows that the detection amplitude exhibited a symmetric response at the defect center. The optimal SNR was observed for 100-150 turns, and it decreased significantly after 175 turns. An increase in the number of turns leads to a higher resistance and inductance, thereby reducing sensitivity. Considering the required magnetic field strength and outer diameter installation constraint (≥1.5 mm), 150 turns were ultimately selected to balance the detection performance with engineering feasibility.

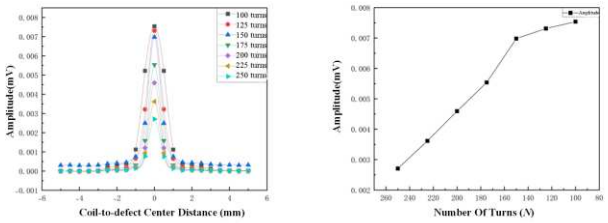



**Fig. 10** Detection signal amplitude diagram and defect signal amplitude diagram corresponding to different coil turns

The wire diameter was further optimized based on an optimal number of 150 turns. The wire diameter was set to range from 0.03 to 0.06 mm (with a step size of 0.005 mm), resulting in the construction of seven simulation models. Fig. 11 shows that the SNR decreases as the wire diameter increases, with stability observed in the 0.03-0.035 mm range, and a significant drop occurring after 0.045 mm. It also indicates that the detection voltage increase is the greatest in the 0.04-0.045 mm range. Considering both the detection sensitivity and process feasibility, 150 turns with a 0.035 mm wire diameter were ultimately selected as the foundation parameters for subsequent simulations.

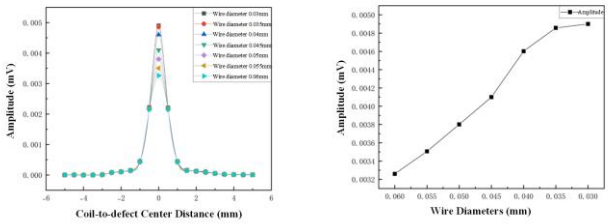



**Fig. 11** Detection signal amplitude diagram and defect signal amplitude diagram corresponding to different wire diameters

Based on Fig. 12, the inner diameter of the eddy current probe was optimized. The detection amplitude was symmetrically distributed, with the highest peak occurring at the center of defect. When the inner diameter ranges from 0.2 to 0.8 mm, the maximum amplitude continuously decreases, with a gradual reduction observed between 0.2 and 0.4 mm and uniform attenuation occurring beyond 0.4 mm. Although the peak value was higher for the 0.2-0.3 mm inner diameter range, the noise was greater, resulting in a lower SNR. The voltage increase in the 0.8-0.4 mm range was 13.2%-13.8%, followed by a sharp drop after 0.4 mm. Considering all factors, an inner diameter of 0.4 mm was selected as the optimal value.

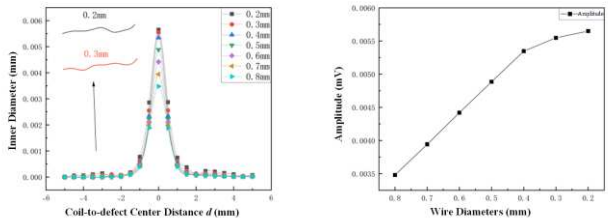



**Fig. 12** Detection signal amplitude diagram and defect signal amplitude diagram corresponding to different inner diameters

After determining the inner diameter of the coil to be 0.4 mm, the parameter of height was further optimized. Simulations were conducted within the range of 0.6 to 1.4 mm (with a step size of 0.2 mm). Fig. 13 shows that the maximum amplitude at the defect center continuously decreases with increasing height, following a pattern of initially rapid decline that slows down as the height increases. Considering both detection sensitivity and process feasibility, a height of 0.8 mm was ultimately selected, balancing the magnetic field penetration capability with the detection sensitivity requirements.

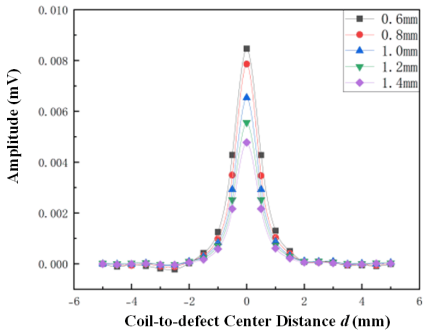



**Fig. 13** Detection signal amplitude diagram corresponding to different heights

Building on the optimized inner diameter of 0.4 mm and height of 0.8 mm, the coil spacing parameter was further optimized. The simulations were set within the range of 0.6 to 2.0 mm (with a step size of 0.2 mm). Fig. 14 shows that the maximum voltage amplitude at the defect center follows a trend of initially increased and then decreased with changes in spacing, with a peak value occurring at 1.0 mm. If the spacing is too small, electromagnetic interference can occur, whereas a spacing that is too large weakens the magnetic coupling. Ultimately, a spacing of 1.0 mm was selected as the optimal value to balance the electromagnetic coupling efficiency and signal fidelity.

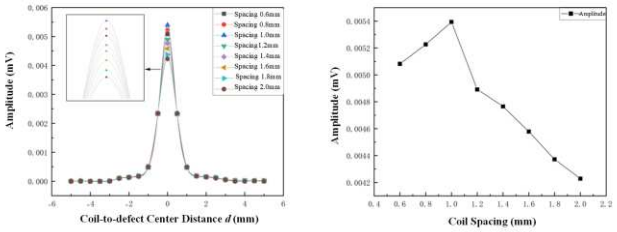



**Fig. 14** Detection signal amplitude diagram and defect signal amplitude diagram corresponding to different coil spacings

The excitation frequency affects the eddy current penetration depth and system impedance through the skin effect. After optimizing the coil parameters, simulations were conducted in an excitation frequency range of 0.8 to 1.45 MHz. It can be found in Fig. 15 that The detection signal amplitude increased with frequency, but the rate of increase gradually slowed: from 0.8 to 1.25 MHz, there was an average increase of 20%, whereas the rate dropped sharply to 0.58% after 1.25 MHz. For the GH3536 nickel-based alloy turbine blades (approximately 0.5 mm in thickness), to ensure detection coverage and avoid signal stalling, an excitation frequency of 1.25 MHz was selected as the optimal value.

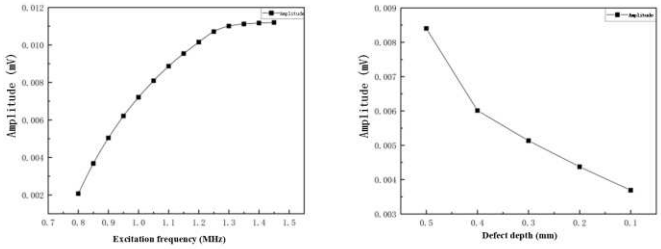



**Fig. 15** Defect signal amplitude diagram corresponding to different frequencies and different depths

The detection capability of an eddy current probe is directly related to the smallest defect size that can be detected. To address the characteristics of cold shut defects extending along the exhaust edge, five groups of simulation experiments were set with varying depths (0.1 mm to 0.5 mm, with a step size of 0.1 mm). Fig. 15 also shows that, as the defect depth increased, the detection signal amplitude decreased. The largest reduction in amplitude occurs in the range from 0.5 mm to 0.4 mm, and beyond 0.4 mm, the rate of decrease slows down.

To address the uncertainty in the direction of the natural defect extension, directional simulations of the eddy current

probe were performed. For comparative analysis ,the defect was placed at the center of a flat plate and the scanning direction of the probe was fixed. The defect angle was rotated from 10° to 90° with a step size of 10°. Fig. 16 shows that the maximum detection voltage amplitude fluctuates between $1.25\times10^{-4}$ V and $1.35\times10^{-4}$ V at all angles, with a maximum difference of only $4.37\times10^{-4}$ V. This indicates that the defect rotation angle had no significant impact on the detection sensitivity.

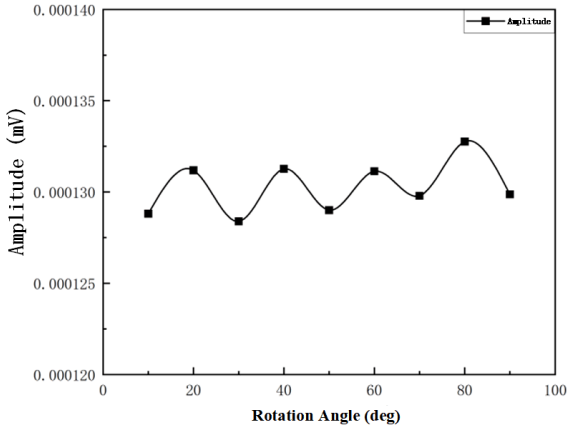



**Fig. 16** Defect signal amplitude diagram corresponding to different angles

Through COMSOL optimization: (1) A circular bridge absolute coil was selected to match the directional characteristics of the cold shut defects in the turbine blades. (2) A comparison between the permalloy 1J85 and manganese-zinc ferrite magnetic cores was conducted, and the latter showed a better SNR. The optimal coil parameters were determined through parameter scanning, which were 150 turns, 0.035 mm wire diameter, 0.4 mm inner diameter, and 1 mm height, with the best detection performance achieved at a spacing of 1 mm. (3) An excitation frequency of 1.25 MHz was selected, considering the blade thickness and skin effect. (4) Verification showed that the probe is sensitive to defect depth but not to directionality.

## 4 Experimental research

### 4.1 Fabrication of specialized probe

The ECT system comprises four main modules: excitation signal generation, detection coil, signal conditioning, and imaging output. Defect visualization was achieved using electromagnetic induction signal analysis. The excitation module generates high-precision signals based on DDS technology combined with an external clock reference and integrates the ICL8038 multi-waveform generator. The frequency/waveform parameters were controlled by adjustable resistors, and the signal was amplified using a TDA2030 power amplifier to drive the detection probe. The probe adopted an optimized circular bridge absolute coil structure, with a composite magnetic core and slender steel tube built-in, designed to meet the detection requirements for small blind areas in the turbine blade exhaust edge. The matching Wheatstone bridge balance circuit effectively suppresses self-interference, compensates for the induced voltage, and significantly improves SNR and detection sensitivity. Finally, a dedicated probe prototype was developed, as shown in Fig. 17.

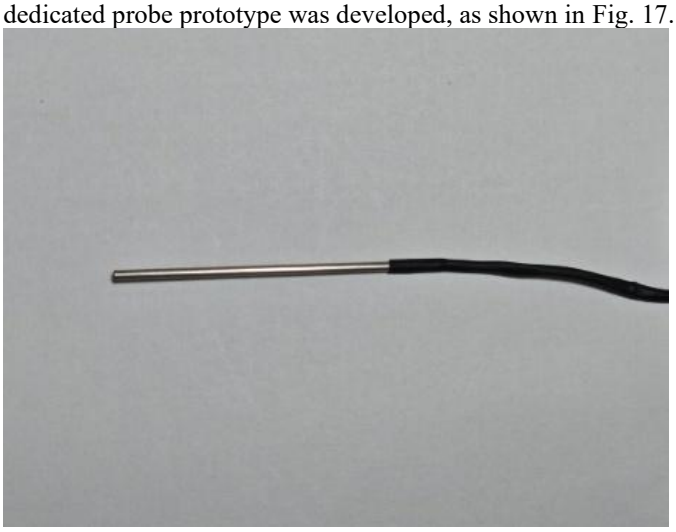


**Fig. 17** Schematic diagram of probe physical object

### 4.2 Design of dual robotic arm ECT system

To address the challenges of detecting the exhaust edge of the turbine blades, an automated ECT system was designed. This system, centered on an industrial personal computer (IPC) and ECT software, integrates industrial robots, a PLC turntable, and a dedicated probe to achieve efficient and stable automated detection. The system consists of five major modules: the software control system manages task scheduling and defect imaging; the robotic motion system carries the probe and performs precise scanning; the PLC turntable component ensures accurate blade transport and positioning; the ECT module integrates a digital tester and an optimized probe; and the peripheral electrical system ensures multi-device coordination. On the hardware side, the IPC sends control commands via TCP/IP, whereas real-time communication between the robot and servo motor turntable is based on Profinet and digital I/O. The probe was adapted to multiple blade models using a quick-change device. The detection process included system initialization, probe calibration, blade clamping, automated scanning, real-time impedance signal feedback, and defect imaging data fusion, ultimately generating an automatic detection report. The system significantly improves the efficiency of batch blade testing and the accuracy of small defect characterization through multi-station collaboration and sequential detection mechanisms, meeting the stringent detection requirements for the complex structure of aeroengine blades.

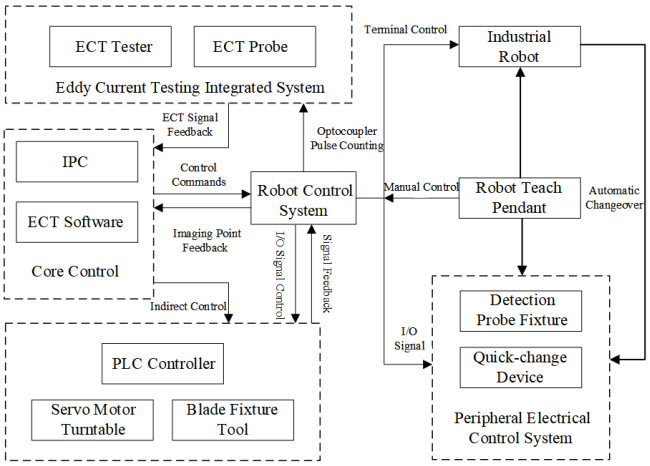



**Fig. 18** Block diagram of overall design scheme

### 4.3 Experimental research

To verify the coverage of the automated detection, three vertical through defects of 0.6 mm×0.1 mm×0.5 mm were machined on the exhaust edge of the blade, one at 1.5 mm from the upper edge, one at 1.5 mm from the lower edge, and one at the middle area. Fig. 19 shows the specimen sample corresponding defect machining drawing.

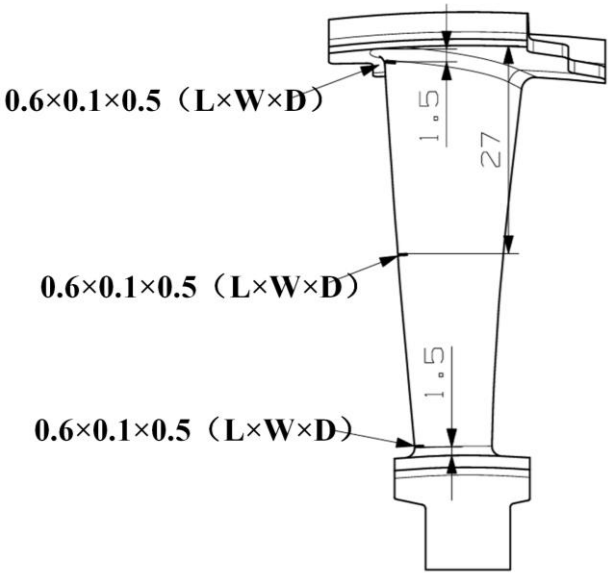



**Fig. 19** defect processing diagram of comparison specimen

This chapter describes experiments conducted by simulating and planning detection paths while optimizing rapid program parameters. After calibrating the tool coordinate system, the system was tested in a real environment. A standard specimen was used to select the optimal path based on time-domain analysis in manual mode, and the stability of the system was verified through the C-scan interface in automatic mode. Further studies were conducted on the impact of the motion parameters, defect size, and orientation on the signal amplitude. Finally, the detection capability of the system is validated using a turbine blade with natural defects. The overall process is illustrated in Fig. 20.

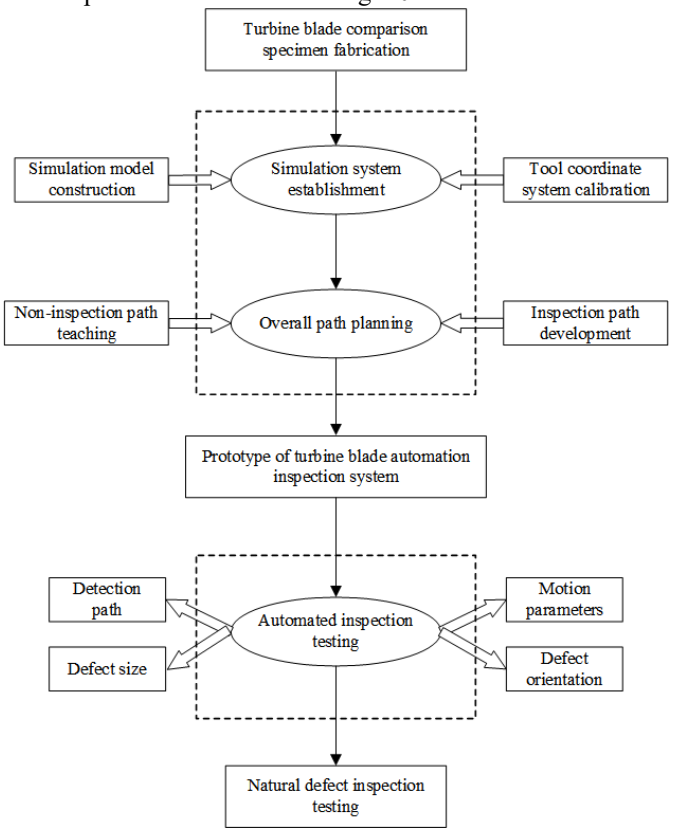



**Fig. 20** Automated testing flowchart for turbine blades

The detection trajectory planning needs to balance the probe attitude changes and noise control, directly affecting the SNR of the ECT. As shown in Fig. 21, defect 2 is located in the middle of the straight section of the exhaust edge, whereas defects 1 and 3 are near the curved regions of the upper and lower edge plates. In the straight section, the probe attitude changes slightly, resulting in low noise; in the curved section, the attitude adjustment is significant, leading to noticeable noise.

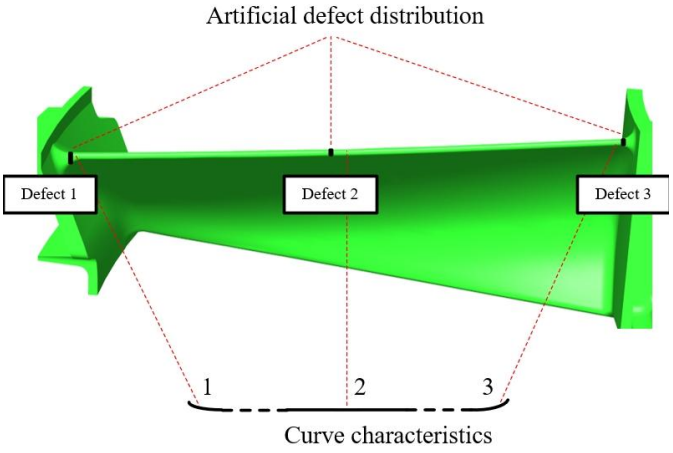



**Fig. 21** Schematic diagram of defect distribution and exhaust edge curve characteristics

The planned path (Fig. 22) extends the attitude change interval. By continuously adjusting the attitude from starting point a to midpoint b, the risk of jitter caused by short-distance changes is reduced, thereby improving the scanning stability. However, the probe may deviate from the normal direction, which can affect the defect detection amplitude.

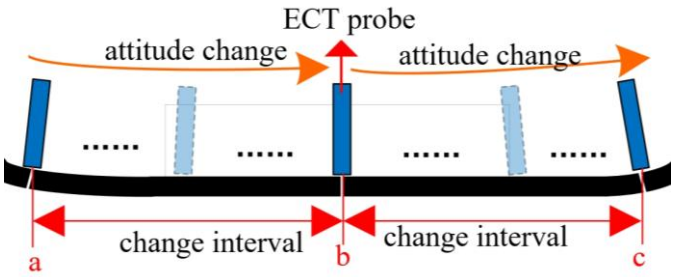



**Fig. 22** Schematic diagram of path and posture transformation

The prototype testing is based on an established automated detection system. In the manual mode, the eddy current detection parameters are adjusted, the phase and gain ratio are tuned to separate interference from defect phases, noise is suppressed through high-pass, low-pass, and digital filtering, and the signal smoothness is optimized. The probe scanning speed was set to 20 mm/s, and the excitation frequency was set to 1.25 MHz. The final detection process parameters were configured as listed in Table 2.

**Table 2** Detection process parameters of automated eddy current system

| Excitation frequency | Excitation voltage | High-pass filtering | Low-pass filtering | Digital filtering | Gain ratio Y/X | Scanning speed |
|---|---|---|---|---|---|---|
| 1.25MHz | 5V | 2Hz | 1000 Hz | 25Hz | 2.4/ 0.8 | 20 mm/s |

Two detection paths were planned for detecting the turbine blade exhaust edge. The first version might increase noise owing to robot jitter caused by short-distance attitude changes. Therefore, an experiment was conducted on the first version of the path using the parameters in Table Ⅱ. The results are presented in Fig. 23.

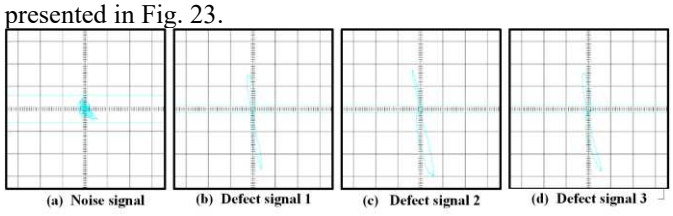



**Fig. 23** ECT results of the first version detection path

To verify the detection effectiveness of the path, three sets of control specimens were added. The distance between defect 1 and the upper edge plate was adjusted to 1.7 mm, 1.9 mm, and 2.1 mm (the original standard specimen was 1.5 mm). By comparing the detection amplitude differences at various defect positions, the changes in detection sensitivity owing to the probe not adhering to the normal direction in real time were analyzed. Relevant defect machining drawings are shown in Fig. 24.

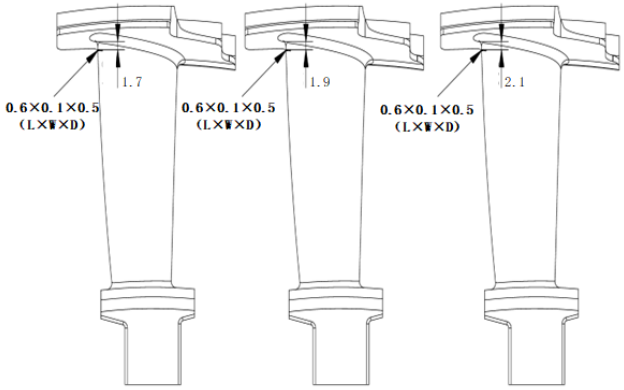



**Fig. 24** Defect processing diagram of comparison specimen

The detection results for the standard comparison specimen (1.5 mm) and the three sets of control specimen (1.7 mm, 1.9 mm, 2.1 mm) are shown in Fig. 25.

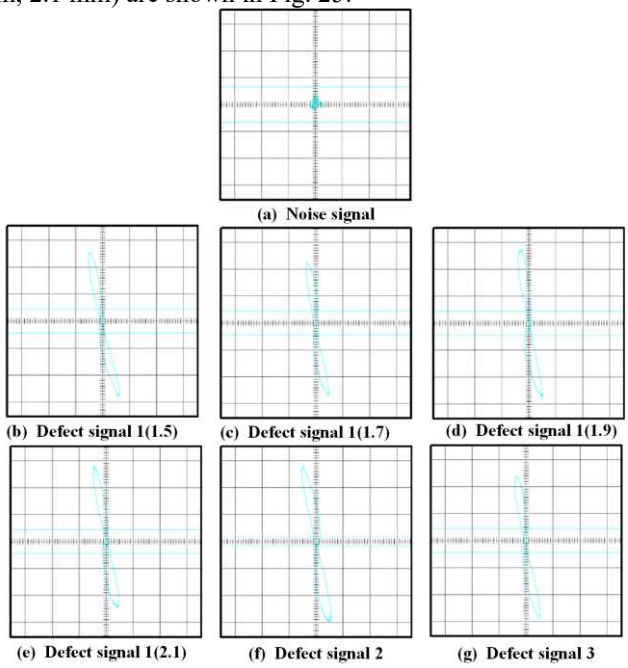



**Fig. 25** ECT results of detection path

The path noise was 33, and the defect detection amplitude fluctuations were small (a maximum difference of 16). The signals for defects 2 and 3 are 268 and 261, respectively, with a comprehensive SNR of 7.3:1. The experiment shows that extending the attitude change interval can reduce robot jitter and improve the SNR. The slight deviation of the probe axis has a limited impact on the detection, making this path effective.

Based on the simulation workstation, the robot speed was adjusted (10-30 mm/s, stepping by 5 mm/s) to test the probe stability. The eddy current signal impedance diagram of defect 2 on the standard specimen was extracted, and the speed-amplitude variation curve was plotted. The results are

presented in Fig. 26.

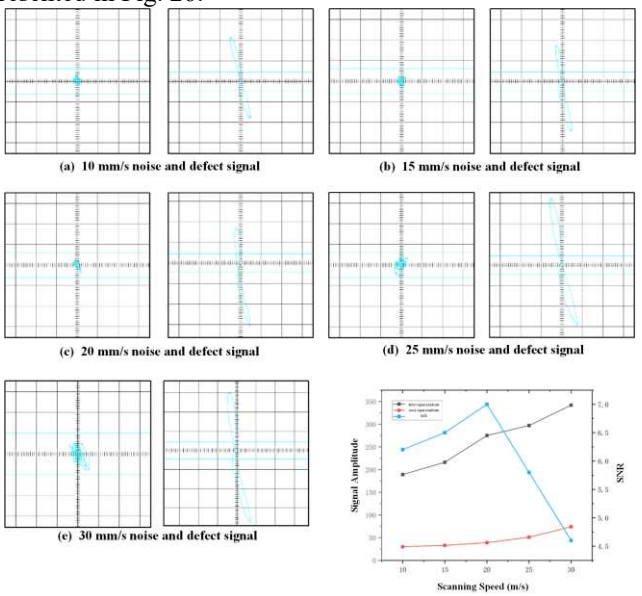



**Fig. 26** Eddy current signal impedance diagram and curve of detection signal amplitude at different scanning speeds

By simulating the adjustment of the probe scanning speed (10-30 mm/s, with a 5 mm/s step), the changes in defect signal 2 on the standard specimen were analyzed. Both the noise and defect amplitudes increased with the speed. However, at 10-20 mm/s, the defect growth rate (19.78%) was faster than the noise growth rate (13.49%). At speeds between 20-30 mm/s, the noise growth rate (37.7%) surpassed the defect growth rate (11.52%), resulting in the SNR first increasing and then decreasing.A peak SNR of 7:1 was obtained at 20 mm/s. Considering both the efficiency and accuracy, a scanning speed of 20 mm/s was chosen as the optimal speed.

The real defects were smaller than the artificial defects on the standard specimen, particularly in terms of depth. Based on this, four sets of control specimen were manufactured with defects of length and width 0.6 mm×0.1 mm and depth ranging from 0.1 mm to 0.4 mm. The corresponding eddy current signal impedance and amplitude variation curves are shown in Fig. 27.

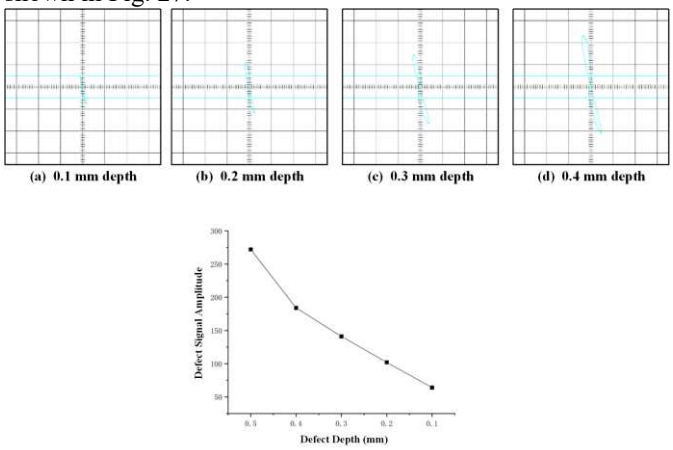



**Fig. 27** Eddy current signal impedance diagram and curve of detection signal amplitude at different defect depths

Fig. 27 shows that the defect depth significantly affected the signal amplitude. The amplitudes corresponding to depths ranging from 0.5 mm to 0.1 mm are 272, 184, 141, 102, and 64, respectively, with the SNR decreasing from 8.2 to 1.9. When the depth is between 0.5 mm and 0.2 mm, the SNR is greater than 3, and the eddy current probe can detect the defects. However, when the depth is less than 0.2 mm, the detection ability significantly decreases.

To verify the effect of the defect inclination angle on the detection signal, nine artificial grooves of size 0.6 mm×0.1 mm×0.5 mm were machined along the exhaust edge of the control specimen. The angles increased by 10° from 0° to 90° (Fig. 28). The eddy current probe was used to scan the exhaust edge at a constant speed, and the maximum signal amplitude was extracted (Fig. 29). The results showed that the defect signal amplitude fluctuated between 251 and 288, with an average of 272 and a standard deviation of approximately 12.89. The maximum difference was 37, indicating that the detection performance of the probe was relatively unaffected by the inclination angle of the defect.

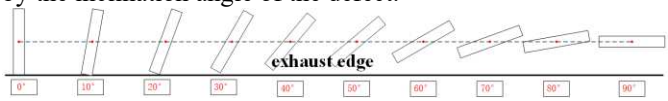



**Fig. 28** Schematic diagram of different defect angles relative to the exhaust edge position

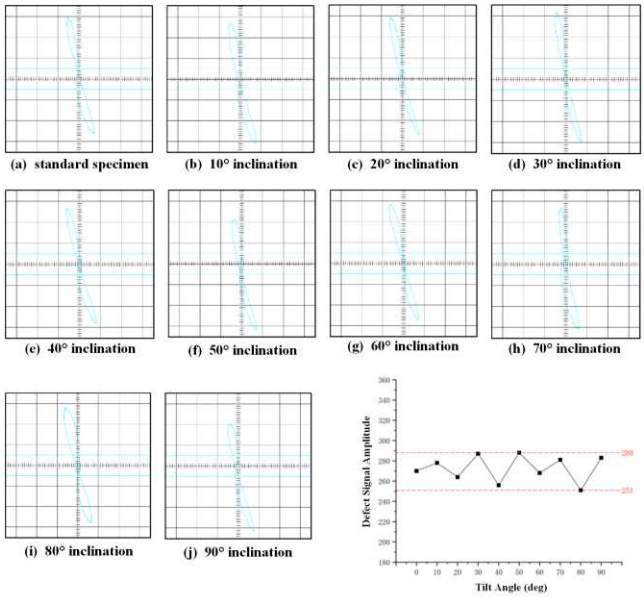
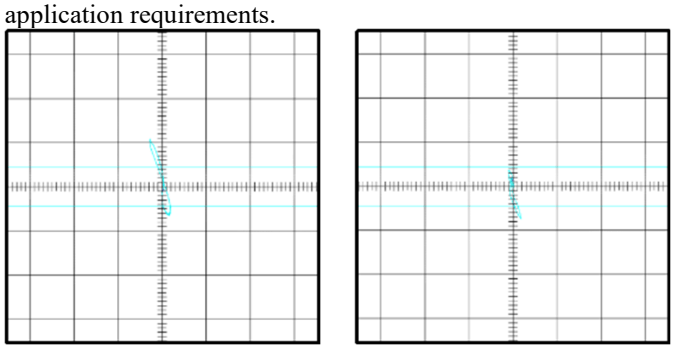



**Fig. 29** Eddy current signal impedance diagram and detection signal amplitude diagram at different defect angles

This study validates the capability of an automated ECT system to detect real natural cracks in turbine blades. Considering the complex morphology and variable signals of natural cracks, as well as the fact that the ECT in the actual process primarily targets cold shut defects with a very low defect rate, tests showed that the blind zone detected by the system was ≤ 1.5 mm. The detection results for the two blades containing natural defects are shown in Fig. 30. The defect signal amplitudes were 87 and 65, with corresponding SNRs

of 2.64 and 1.97, respectively. Although these ratios are lower than those obtained from the artificial groove experiments, setting a critical threshold of 40 effectively distinguishes defects from noise. The defect visualization results (Fig. 31) further confirm the defect localization accuracy, demonstrating that the system is capable of detecting and locating small blind zone natural defects, meeting engineering application requirements.



(a) Blade 1 (b) Blade 2

**Fig. 30** Natural defect eddy current signal impedance diagram

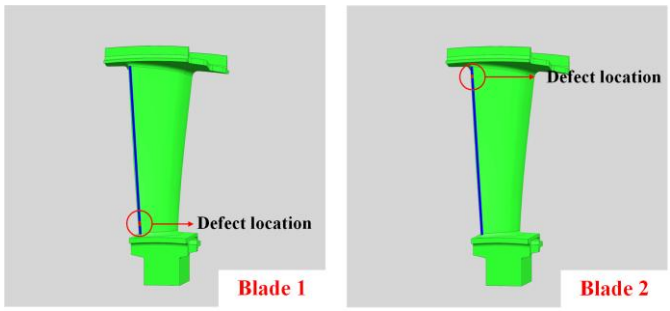



**Fig. 31** defect visualization imaging diagram

## 5 Conclusion

(1) A circular eddy current absolute-type coil edge detection model was constructed using COMSOL, and the probe structure was optimized through parameterized scanning. A manganese-zinc ferrite magnetic core (with an SNR superior to that of permalloy 1J85) was adopted, and the coil parameters were determined to be 150 turns, 0.035 mm wire diameter, 0.4 mm inner diameter, 1 mm height, with a 1 mm spacing and an excitation frequency of 1.25MHz. Simulation results show that the probe is sensitive to defect depth (with an SNR of 8.2 for a 0.5 mm depth), but not sensitive to defect orientation (with a variation of only 37 for angles between 0° and 90°), providing a theoretical basis for automated detection.

(2) An automated detection system was developed, featuring collaboration between an industrial robot and a PLC turntable, integrated with a defect visualization imaging module. Experimental tests showed that the detection SNR was 7.3:1, while maintaining the defect detection capability (with a blind zone verification of 1.5 mm). The system supports an optimal scanning speed of 20 mm/s, which balances the detection efficiency and stability.

(3) For real cold shut defects, the system's blind zone detection is ≤ 1.5 mm. It effectively identified natural defect signal amplitudes (87, 65) with SNR of 2.64 and 1.97. Noise and defects can be effectively distinguished by setting a critical threshold of 40. The imaging results were consistent with the actual defect locations, confirming the system's defect localization accuracy for complex natural defect shapes. The experiment shows that the system can resolve defects with a depth greater than 0.2 mm, with negligible impact from tilt angles, meeting the quality control requirements for turbine blades in aerospace engines.

**Acknowledgements** This work was supported by the industry university research cooperation project of Aero Engine Corporation of China (AECC), the key research and development plan of Jiangxi Province and Jiangxi Provincial Natural Science Foundation (Youth) project.

**Author Contributions** All authors contributed to the study conception and design. Material preparation, data collection and analysis were performed by Kai Song and Wenyu Xie. The first draft of the manuscript was written by Wenyu Xie and all authors commented on previous versions of the manuscript. All authors read and approved the final manuscript.

**Funding** This work was supported by the industry university research cooperation project of Aero Engine Corporation of China (AECC), the key research and development plan of Jiangxi Province and Jiangxi Provincial Natural Science Foundation (Youth) project (Grant numbers HFZL2023CXY029, 20252BCE310030 and 20242BAB20210)

**Data Availability** No datasets were generated or analysed during the current study.

## Declarations

**Conflict of Interest** The authors declare no competing interests.

**Open Access** This article is licensed under a Creative Commons Attribution 4.0 International License, which permits use, sharing, adaptation, distribution and reproduction in any medium or format, as long as you give appropriate credit to the original author(s) and the source, provide a link to the Creative Commons licence, and indicate if changes were made. The images or other third party material in this article are included in the article's Creative Commons licence, unless indicated otherwise in a credit line to the material. If material is not included in the article's Creative Commons licence and your intended use is not permitted by statutory regulation or exceeds the permitted use, you will need to obtain permission directly from the copyright holder. To view a copy of this licence, visit http://creativecommons.org/licenses/by/4.0/.

## References

[1] Y. Zhong, T. Li, S. Qu, H. Huang, and Z. Zhang, "Failure analysis of over-temperature of aeroengine bearing," *J.*

*Fail. Anal. Prev*, vol. 23, no. 5, pp. 1869–1879, Sep, 2023, DOI. 10.1007/s11668-023-01704-w.

[2] B. Lei, N. Shen, D. Ji, R. Ouyang, L. Yang, "A comprehensive review of key technologies for enhancing the reliability of aeroengines," *IEEE Access*, vol. 12, pp. 148315-148331, Oct, 2024, DOI. 10.1109/ACCESS.2024.3474737.

[3] M. Yadav, A.Misra, A. Malhotra, N. Kumar, "Design and analysis of a high-pressure turbine blade in a jet engine using advanced materials," *Mater. Today*, vol. 25, no. 4, pp. 639-645, 2020, DOI. 10.1016/j.matpr.2019.07.530.

[4] H. Liu, J. Sun, S. Lei, S. Ning, "In-service aircraft engines turbine blades life prediction based on multi-modal operation and maintenance data," *propulsion and power research*, vol. 10, no. 4, pp. 360-373, Dec, 2021, DOI. 10.1016/j.jppr.2021.09.001.

[5] X. Hao, G. Liu, Y. Wang, S. Wu, Z. Wang, "Optimization of investment casting process for K477 superalloy aeroengine turbine nozzle by simulation and experiment," *China Foundry*, vol. 19, no. 4, pp. 351-358, Jun, 2022, DOI .10.1007/s41230-022-1092-4.

[6] M. Lakshmi, A. Mondal, C. Jadhav, B. Dutta, S. Sreedhar, "Overview of NDT methods applied on an aero engine turbine rotor blade," *INSIGHT*, vol. 55, no. 9, pp. 482-486, Sep, 2013, DOI. 10.1784/insi.2012.55.9.482.

[7] G. J. Qi, H. Lei, G. Q. Fu, P. Jing, J. M. Lin, "In situ eddy-current testing on low-pressure turbine blades of aircraft engine," *J Test Eval*, vol. 40, no. 4, pp. 553-556, Jul, 2012, DOI. 10.1520/JTE103388.

[8] M. A. Machado, "Eddy currents probe design for NDT applications: a review," *SENSORS-BASEL*, vol. 24, no. 17, pp. 5819,Sep, 2024, DOI. 10.3390/s24175819.

[9] N. M. Angel, A. Basak, "On the fabrication of metallic single crystal turbine blades with a commentary on repair via additive manufacturing," *Journal of Manufacturing and Materials Processing*, vol. 4, no. 4, pp. 101, Oct, 2020, DOI. 10.3390/jmmp4040101.

[10] P. Puspitasari, A. Andoko, P. Kurniawan, "Failure analysis of a gas turbine blade: A review,"in *IOP Conf. Ser.:Mater. Sci. Eng*, Malang, Indonesia, 2021, DOI. 10.1088/1757-899X/1034/1/012156.

[11] J. Krawczyk, R. Paszkowski, W. Bogdanowicz, K. Hanc-Kuczkowska, J. Sieniawski, "Defect creation in the root of single-crystalline turbine blades made of Ni-based superalloy," *Materials*, vol. 12, no. 6, pp. 870, Mar, 2019, DOI. 10.3390/ma12060870.

[12] M. A. Baduhalin, A. S. A. A. Rani, J. Jamil, M. N. F. Saniman, E. M. Yusup, "Development of Efficient Frequency and Sensitivity of Transducer on Flaw Measurement by Using Ultrasonic Testing Method on Thin Carbon Steel Plate," *Int. J. Integr. Eng*,vol. 16, no. 9, pp. 171-181, Apr, 2024, DOI. 10.30880/ijie.2024.16.09.013.

[13] P. Lv, M. Li, X. Su, L. Cheng, H. Ma, "Research on eddy current and force of non-ferrous metal in eddy current separator," *Int. J. Appl. Electromagn. Mech*, vol. 72, no. 3, pp. 279-306, Jun, 2023, DOI. 10.3233/JAE-220143.

[14] J. Ge, B. Hu, C. Yang, F. Yu, N. Yusa, "Surface Profile Reconstruction of Complex Cracks Using the Signals of Rotating Eddy Current Testing Through the Eddy Current Imaging Method," *IEEE Trans. Ind. Electron*, vol. 70, no. 9, pp. 9632-9641, Sep, 2023, DOI. 10.1109/TIE.2022.3206746.

[15] A. V. Egorov, V. V. Polyakov, "Multifrequency Eddy Current Testing of Structural Steel Sheets," *Russ. J. Nondestruct. Test*, vol. 60, no. 11, pp. 1263-1271, Jan, 2024, DOI. 10.1134/S1061830924602277.

[16] J. Yuan, Z. Lei, X. Xue, H. Chen, G. Wen, Y. Su, X. Chen, "Simulation of the Back-Side Cracking of Nickel-Based Superalloy Turbine Blades with Eddy Current Testing," in *MDS 2024*, Springer, Singapore, 2024, pp. 941-956.

[17] H. B. Zhang, C. Y. Zhang, D. J. Cheng, K. L.Zhou, Z. Y. Sun, "Detection Transformer with Multi-Scale Fusion Attention Mechanism for Aero-Engine Turbine Blade Cast Defect Detection Considering Comprehensive Features," *SENSORS-BASEL*, vol. 24, no. 5, pp. 1663, Mar, 2024, DOI. 10.3390/s24051663.

[18] J. Kang, Z. Zeng, "Comparison of skin effects in ferromagnetic and nonferromagnetic metals in eddy current testing," *Res. Nondestr. Eval*, vol. 35, no. 5, pp. 268-282, Sep, 2024, DOI. 10.1080/09349847.2024.2395513.

[19] M. C. C. Monu, J. C. Chekotu, D. Brabazon, "Eddy current testing and monitoring in metal additive manufacturing: A review," *J. Manuf. Process*, vol. 134, pp. 558-588, Jan, 2025, DOI. 10.1016/j.jmapro.2024.12.033.